ADVANCED FUNCTIONAL MATERIALS

www.afm-journal.de

Sol–Gel Synthesis of Robust Metal–Organic Frameworks for Nanoparticle Encapsulation

Joshua P. Mehta, Tian Tian, Zhixin Zeng, Giorgio Divitini, Bethany M. Connolly, Paul A. Midgley, Jin-Chong Tan, David Fairen-Jimenez, and Andrew E. H. Wheatley**

A new type of composite material involving the in situ immobilization of tin oxide nanoparticles (SnO_2-NPs) within a monolithic metal–organic framework (MOF), the zeolitic imidazolate framework (ZIF)-8 is presented. $SnO_2@_{mono}$ZIF-8 exploits the mechanical properties, structural resilience, and high density of a monolithic MOF, while leveraging the photocatalytic action of the nanoparticles. The composite displays outstanding photocatalytic properties and represents a critical advance in the field of treating toxic effluents and is a vital validation for commercial application. Crucially, full retention of catalytic activity is observed after ten catalytic cycles.

1. Introduction

The catalytic degradation of organic molecules such as toxic dye effluents and nerve agents has received considerable attention in recent years.[1] Metal–organic frameworks (MOFs) have been proposed as promising catalysts for the degradation of these compounds. However, the possibility of incorporating catalytic nanoparticles (NPs) to create new functional composites brings vast benefits in terms of their performance. At the same time, the use of MOFs as supports for catalytic NPs has been hindered due to the powder morphology of the former, which results in poor catalyst retention and recyclability. Furthermore, the development of new applications for NPs faces difficulties owing to particle toxicity and agglomeration. Overall, shaping of powdered supports into monolithic conformations has been a long-standing challenge to the applicability of these materials. A satisfactory solution promises to address problems associated with pressure drops in adsorption columns due to MOF powder compaction and to promote the recovery of catalytic NPs from liquid phases.

In the last 20 years, the Cambridge Crystallographic Database Centre has catalogued more than 80 000 MOFs, comprising a vast variety of organic linkers, nodes, and topologies.[2] Despite the burgeoning interest in MOFs and in the improvement of catalytic MOF composites,[3–5] the development of monolithic structures for these multifunctional materials has not been explored thoroughly. Hence, for example, previous work has focused on size control, spatial distribution, and controlled encapsulation of NPs in nanocrystalline MOFs, achieving great success in terms of catalytic performance.[6] However, in a recent major advance in MOF shaping, we presented a novel sol–gel synthetic method for producing transparent, robust, monolithic zeolitic imidazolate framework (ZIF)-8 without the need for high pressures or binders.[7] These *monoliths* are conformed (i.e., shaped) porous structures that retain the same porous texture and chemical/thermal stability of the nanocrystalline MOF[8] but now in the form of a mechanically robust macrostructure with bulk densities and volumetric Brunauer–Emmett–Teller (BET) areas 3–4 times higher than those of the powder. This new approach to MOF synthesis presents multiple advantages over the prior art. First, it has yielded the first conformed porous material that, after successful packing and densification, reached the volumetric DOE target for methane storage.[9] Second, compared with other pelletization methods that can lead to up to 90% of pore collapse and pore blocking due to the use of high pressures,[10] this sol–gel synthetic protocol introduces the possibility of creating mechanically stable monoliths based on porous MOFs that can robustly incorporate highly active and potentially toxic species such as NPs.[11,12]

The incorporation of catalytically active NPs into a MOF represents an important method of exploiting the combined physicochemical properties of both constituents.[11] However, to the best of our knowledge, there are no reports of

J. P. Mehta, B. M. Connolly, Dr. A. E. H. Wheatley
Department of Chemistry
University of Cambridge
Lensfield Road, Cambridge CB2 1EW, UK
E-mail: aehw2@cam.ac.uk

Dr. T. Tian, Dr. D. Fairen-Jimenez
Adsorption and Advanced Materials (AAM) Laboratory
Department of Chemical Engineering & Biotechnology
University of Cambridge
Philippa Fawcett Drive
Cambridge CB3 0AS, UK
E-mail: df334@cam.ac.uk

Z. Zeng, Prof. J.-C. Tan
Department of Engineering Science
University of Oxford
Parks Road, Oxford OX1 3PJ, UK

Dr. G. Divitini, Prof. P. A. Midgley
Department of Materials Science & Metallurgy
University of Cambridge
27 Charles Babbage Road, Cambridge CB3 0FS, UK

The ORCID identification number(s) for the author(s) of this article can be found under https://doi.org/10.1002/adfm.201705588.

DOI: 10.1002/adfm.201705588

NP encapsulation via a "bottom-up" synthesis involving MOF precursors resulting in mechanically stable monolithic composite (NP@$_{mono}$MOF) macrostructures recoverable by simple filtration. Previous attempts to exploit the properties of MOFs for environmental remediation have focused on powdered morphologies, with their ability to degrade toxic organic compounds being poor.[13] Furthermore, compared with other monolithic samples such as 3D graphene aerogel, the preparation of our material is highly time and energy efficient: 10 min reaction at room temperature for the monolithic MOF compared to a 12 h reaction at 90 °C for the graphene aerogel.[14] In this work, we used recent advances in sol–gel synthesis to create a mechanically and chemically robust monolithic MOF able to encapsulate NPs. On the one hand, we chose the prototypical ZIF-8 ($Zn(2\text{-}mIm)_2$, 2-mIm = $C_4H_5N_2^-$) MOF from the ZIF family.[15] ZIF-8 shows a sodalite topology with large cages and narrow windows (1.16 nm cavity diameter and flexible 0.34 nm windows),[16] boasting both high porosity (total pore volume 0.485 $cm^3\ g^{-1}$) and high chemical and thermal stability.[17] On the other hand, we chose SnO_2-NPs for encapsulation due to their nontoxic nature and track record in detoxification.[18] In addition, despite the proven benefits of SnO_2-NPs in the photocatalytic degradation of toxic molecules, they still present major challenges of recovery and reuse owing to their small size.[19] The SnO_2@$_{mono}$ZIF-8 composite developed here combines excellent activity in the degradation of toxic industry effluent with straightforward catalyst recyclability.

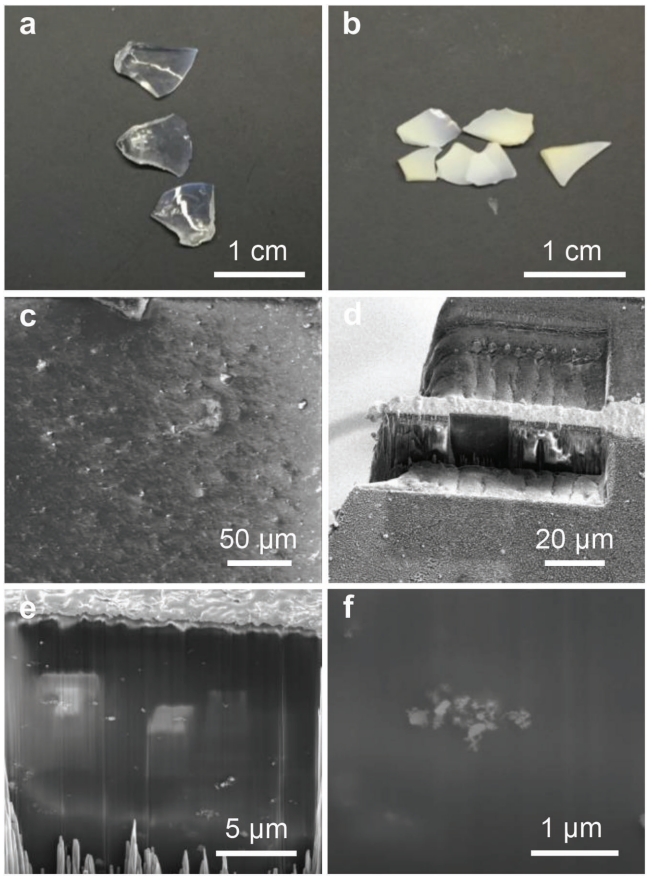

Figure 1. Representative images of a) $_{mono}$ZIF-8 and b) SnO_2@$_{mono}$ZIF-8. c–f) SEM microscopic images of SnO_2@$_{mono}$ZIF-8 upon focused ion beam milling, with the sample at 52° tilt reveal f) embedded SnO_2-NPs; scale bars 1 cm, panels (a, b); 50 µm, panel (c), 20 µm, panel (d); 5 µm, panel (e), and 1 µm, panel (f). Bright rectangular areas and vertical curtaining in panel (e) are due to localized charging under the electron beam and artifacts caused by milling, respectively.

2. Results and Discussion

The synthesis of SnO_2-NPs resulted in uniform, monocrystalline NPs with a mean size distribution of 5.0 ± 1.1 nm and a band gap of 3.74 eV (Figures S1–S4, Supporting Information). We then incorporated them into high-density ZIF-8 monoliths during a sol–gel process similar to the synthesis of monolithic aerogels.[20] This sol–gel process involves the formation of small primary ZIF-8 particles that aggregate, forming the gel macrostructure before being dried into a monolithic structure. Whereas pure ZIF-8 monoliths ($_{mono}$ZIF-8) were transparent (**Figure 1**a), SnO_2@$_{mono}$ZIF-8 appeared white (Figure 1b). Scanning electron microscopy (SEM) analysis of SnO_2@$_{mono}$ZIF-8 revealed a similar flat surface morphology to that previously reported for $_{mono}$ZIF-8 (Figure 1c).[7] Transmission electron microscopy (TEM) analysis of the mother liquor revealed a primary particle size for SnO_2@$_{mono}$ZIF-8 (100–150 nm) larger than that for $_{mono}$ZIF-8 (60–80 nm) (Figure S5, Supporting Information), suggesting that ZIF-8 exhibits slower nucleation in the presence of SnO_2–NPs.[21]

We confirmed the composition of SnO_2@$_{mono}$ZIF-8 using energy-dispersive X-ray spectroscopy (EDX). **Figure 2** shows representative scanning transmission electron microscopy (STEM) images, indicating the presence of bright spots within the monolithic matrix. These present some agglomeration at the local level but are well distributed through the monolith. By using EDX, we confirmed the chemical nature of these bright spots (Figure 2c), so demonstrating the successful encapsulation of SnO_2-NPs.

We further investigated the subsurface features of the monolith and the presence of the SnO_2-NPs, using focused ion beam (FIB)-SEM. Figure 1c–f shows images obtained during etching, revealing SnO_2 agglomerates dispersed throughout the monolithic matrix. By providing a solid surface to which NPs with high interfacial energies can adhere, $_{mono}$ZIF-8 has prevented the worst excesses of NP agglomeration (Figure S1, Supporting Information). Triplicated inductively coupled plasma-optical emission spectroscopy (ICP-OES) experiments found the level of SnO_2-NP loading to be 2.0 ± 0.1 wt% (Table S1, Supporting Information). Attempts to increase the loading of NPs in the composite failed to afford a monolith, suggesting that the 2.0 wt% loading of SnO_2 NPs represents the maximum attainable while preserving the structural integrity of the composite. X-ray photoelectron spectroscopy (XPS) confirmed the results of FIB-SEM. **Figure 3**a shows the FIB-XPS analysis of the 3d region of Sn(IV). This revealed peaks attributable to Sn($3d_{5/2}$) and Sn($3d_{3/2}$) binding energies, centred at 486.7 and 495.5 eV, respectively, confirming the presence of SnO_2.[22] The high-energy shoulder on the Sn($3d_{3/2}$) peak is attributed to the presence of ZIF-8.[23] Encouragingly, we detected Sn consistently throughout etched areas, while the external surface spectrum revealed a lower Sn presence. This supports the FIB-SEM microscopic image and confirms that the majority of SnO_2 is located within the monolith. Discussion of the remaining XPS data may be found in the supporting information (Figures S6 and S7, Supporting Information).

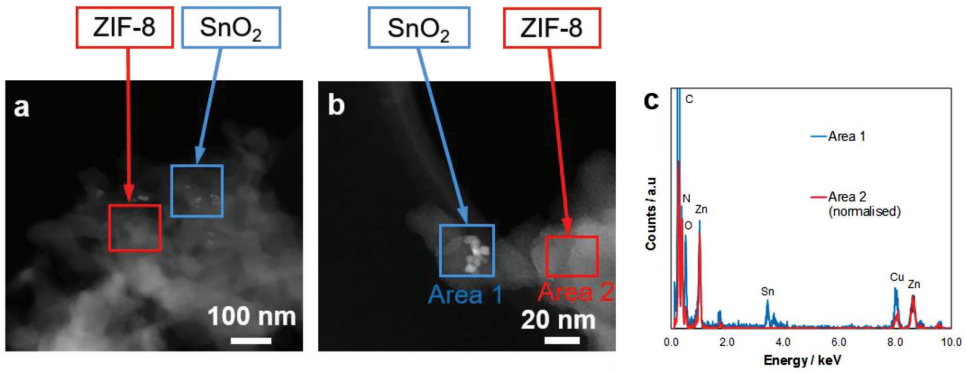

Figure 2. a,b) Representative STEM-HAADF images of SnO_2@$_{mono}$ZIF-8. (Scale bars 100 nm, panel (a) and 20 nm, panel (b).) c) Drift-corrected EDX analysis of SnO_2@$_{mono}$ZIF-8, scanned over Area 1 (blue) and Area 2 (red) as illustrated by the regions defined, panel (b).

Figure 3b compares the powder X-ray diffraction (PXRD) patterns of simulated ZIF-8 with experimental $_{mono}$ZIF-8, SnO_2-NPs, and SnO_2@$_{mono}$ZIF-8. Fresh SnO_2@$_{mono}$ZIF-8 revealed minimal peak variation compared with $_{mono}$ZIF-8, confirming that the SnO_2-NPs do not perturb the crystallinity of the MOF. Figure 3c shows the N_2 adsorption isotherms for the composite; **Table 1** compares the BET areas, and the micropore and total pore volumes. Both $_{mono}$ZIF-8 and SnO_2@$_{mono}$ZIF-8 display typical stepped ZIF-8 adsorption isotherms and an absence of mesoporosity, as confirmed by the similarity of micropore and total pore volumes.[16] However, the adsorption capacity and BET area of the composite are ≈25% lower than those of $_{mono}$ZIF-8. This is attributed to pore blocking by nonporous phases. Mercury porosimetry revealed the bulk density (envelop

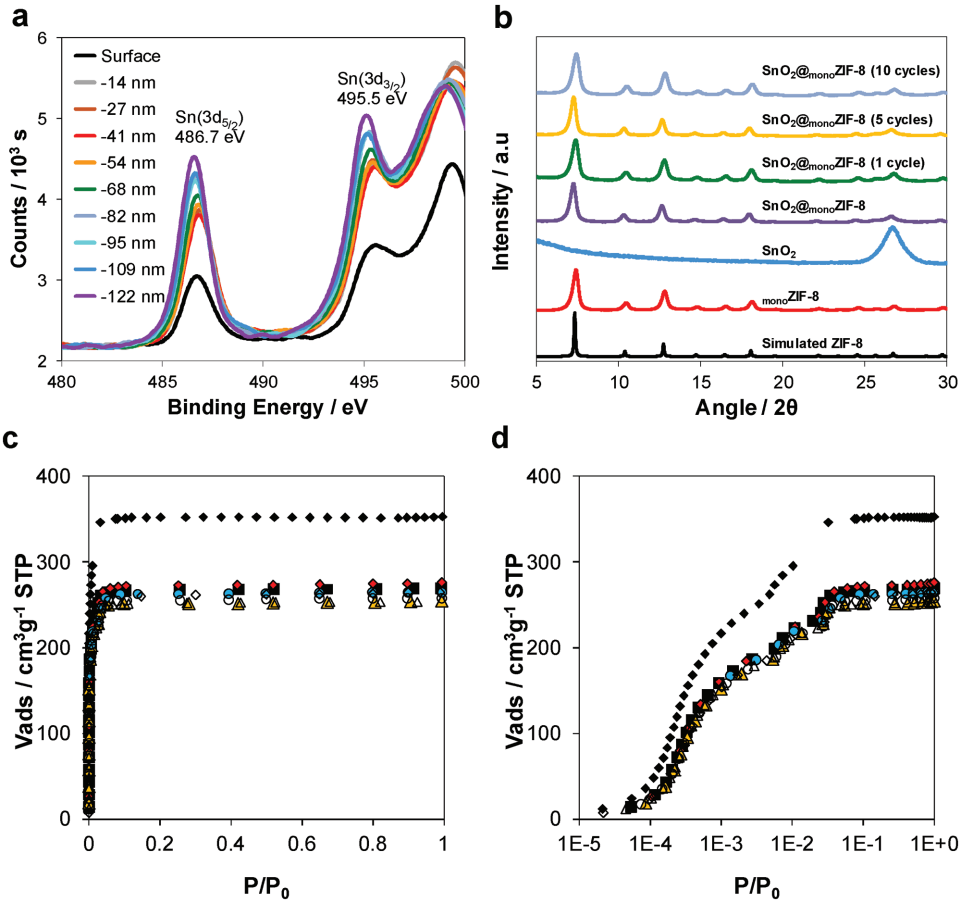

Figure 3. a) FIB-XPS binding energy spectra for the 3d region of Sn(IV) in SnO_2@$_{mono}$ZIF-8; quoted peak energies calculated as an average over the ten spectra. b) PXRD patterns of simulated ZIF-8 and experimental $_{mono}$ZIF-8, SnO_2-NPs, and SnO_2@$_{mono}$ZIF-8 fresh and after 1, 5, and 10 catalytic cycles. N_2 adsorption isotherms at 77 K for $_{mono}$ZIF-8 (◆); SnO_2@$_{mono}$ZIF-8 (■); SnO_2@$_{mono}$ZIF-8 after 1 catalytic cycle (◆); SnO_2@$_{mono}$ZIF-8 after 5 catalytic cycles (▲); SnO_2@$_{mono}$ZIF-8 after 10 catalytic cycles (●); SnO_2@$_{mono}$ZIF-8 after 1 water cycle (◇); SnO_2@$_{mono}$ZIF-8 after 5 water cycles (△); SnO_2@$_{mono}$ZIF-8 after 10 water cycles (○) on c) nonlogarithmic and d) semilogarithmic axes.

Table 1. BET areas (S_{BET}), micropore volumes (W_0), and total pore volumes (V_{TOT}) for $_{mono}$ZIF-8 and SnO_2@$_{mono}$ZIF-8 before and after exposure to methylene blue (MB) and H_2O.

Material	S_{BET} [m^2 g^{-1}]	W_0[a)] [cm^3 g^{-1}]	V_{TOT}[b)] [cm^3 g^{-1}]
$_{mono}$ZIF-8	1423	0.543	0.546
SnO_2@$_{mono}$ZIF-8	1055	0.413	0.417
SnO_2@$_{mono}$ZIF-8—1 cycle (MB)	1068	0.421	0.427
SnO_2@$_{mono}$ZIF-8—5 cycles (MB)	985	0.389	0.393
SnO_2@$_{mono}$ZIF-8—10 cycles (MB)	1027	0.405	0.411
SnO_2@$_{mono}$ZIF-8—1 cycle (H_2O)	973	0.384	0.389
SnO_2@$_{mono}$ZIF-8—5 cycles (H_2O)	991	0.389	0.393
SnO_2@$_{mono}$ZIF-8—10 cycles (H_2O)	996	0.395	0.399

[a)]Data obtained at $P/P_0 = 0.1$; [b)]$P/P_0 = 0.99$.

or particle density) of SnO_2@$_{mono}$ZIF-8 to be slightly higher than that of $_{mono}$ZIF-8, i.e., 1.13 g cm^{-3} versus 1.05 g cm^{-3}, while confirming the absence of meso- and macroporosity (Figure S8, Supporting Information).

2.1. Photocatalytic Studies

As proof of concept to evaluate the photocatalytic activity and, most importantly, the straightforward recovery and reusability of SnO_2@$_{mono}$ZIF-8 for toxic organic molecule destruction, we monitored the catalytic degradation of aqueous methylene blue (MB) solutions over multiple catalytic cycles. Each cycle lasted 3 h, with the composite recovered each time by simple gravity filtration (Figure S9, Supporting Information) before being reused without washing. The degree of degradation was calculated according to the reduction in absorption for the major MB absorption band at $\lambda_{max} = 664$ nm

$$\text{Degradation}[\%] = 100 \times \left(1 - \frac{C_t}{C_0}\right) \quad (1)$$

where C_0 is the initial concentration of MB and C_t is the concentration of MB after time t.

MB (dimensions: 7.9 × 16.3 × 4.0 Å)[24] is widely used in the textile industry and represents a common toxic effluent in water supplies.[25] By using a dye larger than the apertures of ZIF-8 (i.e., 3.4 Å),[16] we have explored the accessibility of the SnO_2-NPs. **Figure 4** shows the degradation of MB in the presence of different amounts of SnO_2@$_{mono}$ZIF-8.

A number of MOFs are known to exhibit photocatalytic properties,[26] with the partial degradation of MB under nanoparticulate ZIF-8 previously attributed to the wide band gap of this semiconducting material.[27] For these reasons, it was essential to establish whether $_{mono}$ZIF-8 represented a potential source of dye degradation in this work. Triplicated control experiments revealed that $_{mono}$ZIF-8 presents no photocatalytic behavior under simulated solar irradiation, with measured dye degradation attributable to surface physisorption (Figures S10 and S11, Supporting Information). Meanwhile, low loading experiments utilizing 0.4 g of composite (i.e., 53 µmol of SnO_2-NPs) proved SnO_2@$_{mono}$ZIF-8 to be moderately photoactive, with an average of 41.5 ± 3.0% MB degradation achieved in 3 h. Importantly, the catalytic performance was sustained, with 39.4 ± 0.6% MB degradation achieved in the 10th cycle, providing compelling evidence for NP retention by the composite (Figure S12, Supporting Information). When increasing the loading to 1.7 g of composite (i.e., 225 µmol catalyst), MB degradation increased to

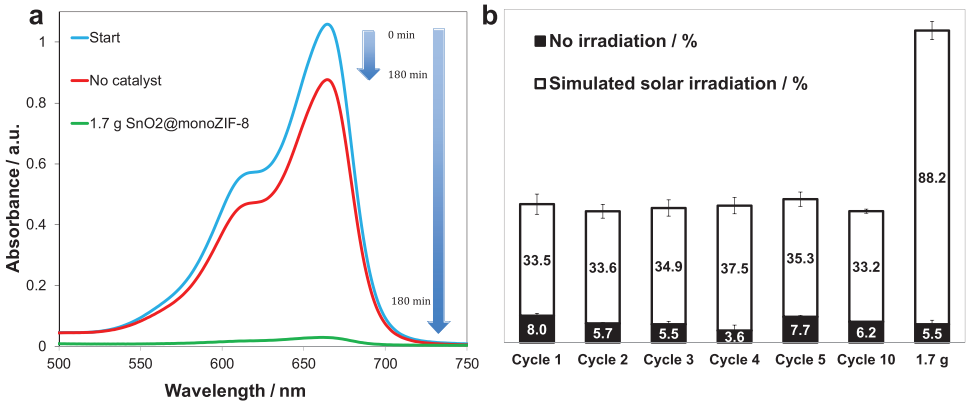

Figure 4. a) Photocatalytically induced spectral changes to aqueous MB dye (1.55×10^{-5} M) highlighting degradation of the absorption maximum at 664 nm in the absence of composite (red) and presence of 1.7 g SnO_2@$_{mono}$ZIF-8 (green) after 3 h of simulated solar irradiation. b) Degradation of MB in the presence of 0.4 g (cycles 1–5 and 10) and 1.7 g of SnO_2@$_{mono}$ZIF-8. Error bars are the standard deviation in triplicated readings.

93.6 ± 2.7% in 3 h. This is a substantial improvement on previously reported semiconducting NP-(ZIF-8) hybrid materials.[13,28] Previous studies suggest that to achieve appreciable degradation of a dye under comparable conditions, 150–300 µmol of powdered photocatalytic NPs are typically required.[29,30]

Interestingly, although the narrow apertures of ZIF-8 preclude the passage of MB, this is not a barrier to photocatalysis. Houas et al. have proposed the following mechanism,[25] where intimate contact between SnO_2-NPs and dye is not necessary:

$SnO_2 + h\nu \rightarrow e^-_{CB} + h^+_{VB}$	1) Exciton production
$O_2 + e^-_{CB} \rightarrow O_2^{\bullet -}$	2) Ionosorption and reduction of O_2 (0 to –0.5 eV)
$H_2O + h^+_{VB} \rightarrow H^+ + OH^\bullet$	3) Production of hydroxyl radicals
$O_2^{\bullet -} + H^+ \rightarrow HO_2^\bullet$	4) Neutralization of $O_2^{\bullet -}$
$2HO_2^\bullet \rightarrow H_2O_2 + O_2$	5) H_2O_2 formation
$H_2O_2 + e^-_{CB} \rightarrow OH^\bullet + OH^-$	6) H_2O_2 degradation
$R + OH^\bullet \rightarrow R'^\bullet + H_2O$	7) Oxidation of dye (R)

In this mechanism, the species active in dye degradation derive from adsorbed oxygen and water.[19] Even allowing for their flexibility, the narrowness of the 3.4 Å windows of ZIF-8 suggests that the dye cannot pass through its framework apertures. This considered, we propose that water, with a 2.68 Å kinetic diameter,[31] diffuses through the ZIF-8 windows[32] and interacts with SnO_2. Reaction with the photoinduced excitons (electrons, e^-, and holes, h^+) in the conduction (CB) and valence (VB) bands of the NPs then creates the hydroxyl and superoxide radicals required for dye degradation. A terephthalic acid (TA) probe was used to determine $OH^\bullet$ radical production. Reaction of TA with $OH^\bullet$ radicals generates the fluorescent species 2-hydroxyterephthalic acid (2-HTA), and the formation of this molecule was monitored using the intensity maximum at 450 nm after excitation at 315 nm. The production of 2-HTA was seen to increase with solar irradiation time (Figure S13, Supporting Information), indicating the photogeneration of $OH^\bullet$ and strongly endorsing the photocatalytic mechanism proposed. Furthermore, the high levels of photocatalytic activity achieved using SnO_2@$_{mono}$ZIF-8 suggest that SnO_2 far below the monolith surface, and not only that present at the external surface, must be intrinsically involved in the catalytic cycle.

We evaluated the chemical robustness of SnO_2@$_{mono}$ZIF-8 by PXRD and N_2 adsorption. PXRD patterns of the composite after 1, 5, and 10 photocatalytic cycles showed no significant variations from that of fresh composite (Figure 3). However, the adsorption isotherms of N_2 showed a small decrease in the BET area (Table 1; Figure 3c,d). We obtained similar values of decrease in BET areas when measuring the adsorption properties of fresh composite after submersion in water for 3 h cycles, suggesting that the decrease is due to the decomposition of SnO_2@$_{mono}$ZIF-8 in water rather than MB adsorption. These data are consistent with ICP-OES data on cycled samples, which showed a relative increase in the loading of Sn due to the loss of zeolitic material (Table S1, Supporting Information). The consistent levels of MB dye degradation up to and including the 10th catalytic cycle (Figure 4b), and the lack of NP leaching as evidenced by ICP-OES on cycled samples (Table S1, Supporting Information), however, suggest that the level of decomposition is very limited and does not affect NP accessibility.

Industrial applications require that materials possess the mechanical strength and toughness to withstand the stresses of friction, cyclic compression, or vibration within a container. We used the nanoindentation technique to establish that the magnitudes of both the Young's modulus, *E*, and Hardness, *H*, of SnO_2@$_{mono}$ZIF-8 (3.30 ± 0.01 and 0.44 ± 0.01 GPa, respectively) were ≈10% greater than those of $_{mono}$ZIF-8 (3.00 ± 0.01 and 0.41 ± 0.01 GPa, respectively), thereby rendering the composite structurally stiffer and more resistant to permanent deformation than pure $_{mono}$ZIF-8 (Figures S14–S17, Supporting Information). This is likely attributable to the incorporation of the SnO_2-NPs leading to a greater packing efficiency of the primary particles.[33]

The thermal stability of fresh and recycled SnO_2@$_{mono}$ZIF-8 was measured by thermogravimetric analysis (TGA) (**Figure 5**). We found that the decomposition temperature for SnO_2@$_{mono}$ZIF-8 (450–500 °C) is lower than that of $_{mono}$ZIF-8 (600 °C). This is expected due to the NPs disrupting the coordination bonds within the MOF.[34] Initial weight losses of 2.5%, 4.0%, 4.5%, 4.5%, and 5.5% at 250 °C for $_{mono}$ZIF-8, fresh SnO_2@$_{mono}$ZIF-8, and SnO_2@$_{mono}$ZIF-8 after 1, 5, and 10 catalytic cycles, respectively, were seen (Figure S18, Supporting Information). As SnO_2 is very thermally stable, these initial weight losses were attributed to ethanol and water adhered to the pure NPs and trapped in the composite materials. Importantly, however, the thermal stability of the composite far exceeded the application temperature and was not reduced after recycling.

To assess the generalization of the encapsulation method, other catalytically active NPs were trialed in the formation of monolithic composites. CdSe and (Au@PdO)/TiO_2 were prepared using modified literature procedures[35–37] and successfully incorporated in $_{mono}$ZIF-8, forming structurally resilient composites (Figures S19 and S20, Supporting Information). Hence, for example, optical imaging shows a change in the color from transparent $_{mono}$ZIF-8 (Figure 1a) to deep red in CdSe@$_{mono}$ZIF-8, showing that the monolith has adopted the color of the NPs. The TEM microscopic image shows the homogeneous distribution of NPs in the MOF matrix, while the PXRD pattern confirms the crystallinity of the sample (Figure S19b–c, Supporting Information).

3. Conclusion

In summary, we report a chemically and mechanically robust composite in which SnO_2-NPs have been controllably integrated into a monolithic MOF without the need for binders, additives, or high pressures, so avoiding structural amorphization and pore collapse. SnO_2@$_{mono}$ZIF-8 has shown high levels of photocatalytic activity and extraordinary recyclability when compared to powdered NPs or previously reported NP@MOF composites. Furthermore, the straightforward synthetic method used led to the entrapment of NPs in a way that prevented catalyst leaching. The outstanding level of recyclability coupled with the unprecedented degree of dye degradation seen under high loading of the composite has proven SnO_2@$_{mono}$ZIF-8 to be a highly effective photocatalyst. The catalytic mechanism proposed involves the diffusion of water through the apertures of ZIF-8 before interaction with the photoactive NPs, exploiting the size selective properties of the MOF. This insight has inspired new avenues of

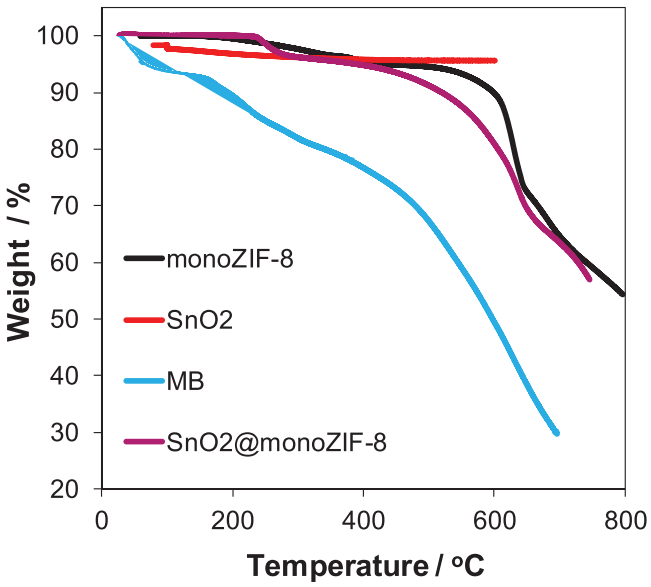

Figure 5. Thermogravimetric analysis of $_{mono}$ZIF-8, SnO_2-NPs, methylene blue (MB), and SnO_2@$_{mono}$ZIF-8.

research in NP@MOF catalysis in which size selectivity of substrates and ease of catalyst recovery are paramount in order to avoid the poisoning and loss of expensive NP catalysts.

4. Experimental Section

Synthesis of SnO_2 Nanoparticles: SnO_2-NPs were prepared following a modified literature synthesis.[38] $SnCl_4{\cdot}5H_2O$ (0.787 g, 2.24 mmol) was dissolved in water (15 mL). Sodium hydroxide (0.7 g, 17.5 mmol) was dissolved in water (20 mL) and ethanol (20 mL). This was added dropwise to the stannic chloride solution until a pH of 12 was achieved. The mixture was transferred quantitatively (≈40 mL) to an autoclave and hydrothermally treated (200 °C, 24 h). After cooling, the resultant precipitate was separated and washed with water and 1:1 ethanol/water mix under centrifugation (7000 rcf). The washed sample was dried in a desiccator overnight, yielding SnO_2-NPs as a white powder.

Synthesis of NP@$_{mono}$ZIF-8 Monoliths: In a representative synthesis, $Zn(NO_3)_2{\cdot}6H_2O$ (0.293 g, 0.985 mmol) was dissolved in ethanol (20 mL). 2-Methylimidazole ($C_4H_6N_2$) (0.809 g, 9.85 mmol) was dissolved separately in ethanol (20 mL), and NPs were added (30 mg). Both solutions were ultrasonicated for 20 min before being combined. The resulting mixture was stirred for 15 min at room temperature and then centrifuged (4250 rcf, 10 min). The collected solid was washed in ethanol (20 mL, three times) and the pellet dried at room temperature overnight, yielding a solid monolith. This was ground into 1–5 mm pieces before activation at 110 °C in a vacuum oven overnight.

Supporting Information

Supporting Information is available from the Wiley Online Library or from the author.

Acknowledgements

J.P.M. and T.T. contributed equally to this work. This work was funded by an EPSRC IAA Partnership Development Award (RG/75759). D.F.-J. thanks the Royal Society for funding through a University Research Fellowship. B.M.C. thanks the Ernest Oppenheimer Fund (Cambridge) for financial assistance. Thanks go also to Dr. Jill Geddes of Schlumberger Gould Research for help with the acquisition of XPS data. Detailed supporting data for this paper are available at the University of Cambridge data repository (see https://doi.org/10.17863/CAM.16995).

Conflict of Interest

The authors declare no conflict of interest.

Keywords

catalyst recovery, composites, metal–organic frameworks, nanoparticles, photocatalysis

Received: September 26, 2017
Revised: November 14, 2017
Published online: January 12, 2018

[1] N. S. Bobbitt, M. L. Mendonca, A. J. Howarth, T. Islamoglu, J. T. Hupp, O. K. Farha, R. Q. Snurr, *Chem. Soc. Rev.* **2017**, *46*, 3357.
[2] P. Z. Moghadam, A. Li, S. B. Wiggin, A. Tao, A. G. P. Maloney, P. A. Wood, S. C. Ward, D. Fairen-Jimenez, *Chem. Mater.* **2017**, *29*, 2618.
[3] G. Lu, S. Li, Z. Guo, O. K. Farha, B. G. Hauser, X. Qi, Y. Wang, X. Wang, S. Han, X. Liu, J. S. DuChene, H. Zhang, Q. Zhang, X. Chen, J. Ma, S. C. J. Loo, W. D. Wei, Y. Yang, J. T. Hupp, F. Huo, *Nat. Chem.* **2012**, *4*, 310.
[4] Y.-B. Huang, J. Liang, X.-S. Wang, R. Cao, *Chem. Soc. Rev.* **2017**, *46*, 126.
[5] D. Rodríguez-San-Miguel, A. Yazdi, V. Guillerm, J. Pérez-Carvajal, V. Puntes, D. Maspoch, F. Zamora, *Chem. – Eur. J.* **2017**, *23*, 8623.
[6] B. Rungtaweevoranit, J. Baek, J. R. Araujo, B. S. Archanjo, K. Min Choi, O. M. Yaghi, G. A. Somorjai, *Nano Lett.* **2016**, *16*, 7645.
[7] T. Tian, J. Velazquez-Garcia, T. D. Bennett, D. Fairen-Jimenez, *J. Mater. Chem. A* **2014**, *3*, 2999.
[8] Y. Gao, J. Wu, W. Zhang, Y. Tan, J. Zhao, B. Tang, *Mater. Lett.* **2014**, *128*, 208.
[9] T. Tian, Z. Zeng, D. Vulpe, M. E. Casco, G. Divitini, P. A. Midgley, J. Silvestre-Albero, J.-C. Tan, P. Z. Moghadam, D. Fairen-Jimenez, *Nat. Mater.* https://doi.org/10.1038/nmat5050.
[10] A. Ahmed, M. Forster, R. Clowes, P. Myers, H. Zhang, *Chem. Commun.* **2014**, *50*, 14314.
[11] T. Berger, O. Diwald, in *Photocatalysis: Fundamentals and Perspectives* (Eds: J. Schneider, D. Bahnemann, J. Ye, G. L. Puma, D. D. Dionysiou), Royal Society of Chemistry, Cambridge **2016**, pp. 185–217.
[12] C. Mongin, S. Garakyaraghi, N. Razgoniaeva, M. Zamkov, F. N. Castellano, *Science* **2016**, *351*, 365.
[13] T. T. Isimjan, H. Kazemian, S. Rohani, A. K. Ray, *J. Mater. Chem.* **2010**, *20*, 10241.
[14] H. Seema, K. C. Kemp, V. Chandra, K. S. Kim, *Nanotechnology* **2012**, *23*, 355705.
[15] Y. Liu, Y. Ma, Y. Zhao, X. Sun, F. Gándara, H. Furukawa, Z. Liu, H. Zhu, C. Zhu, K. Suenaga, P. Oleynikov, A. S. Alshammari, X. Zhang, O. Terasaki, O. M. Yaghi, *Science* **2016**, *351*, 365.
[16] D. Fairen-Jimenez, S. A. Moggach, M. T. Wharmby, P. A. Wright, S. Parsons, T. Düren, *J. Am. Chem. Soc.* **2011**, *133*, 8900.

[17] D. Fairen-Jimenez, R. Galvelis, A. Torrisi, A. D. Gellan, M. T. Wharmby, P. A. Wright, C. Mellot-Draznieks, T. Düren, *Dalton Trans.* **2012**, *41*, 10752.
[18] A. Kar, A. Patra, *J. Mater. Chem. C* **2014**, *2*, 6706.
[19] A. Kar, S. Sain, D. Rossouw, B. R. Knappett, S. K. Pradhan, A. E. H. Wheatley, *Nanoscale* **2016**, *8*, 2727.
[20] D. Fairen-Jimenez, F. Carrasco-Marín, C. Moreno-Castilla, *Langmuir* **2008**, *24*, 2820.
[21] J. Cravillon, R. Nayuk, S. Springer, A. Feldhoff, K. Huber, M. Wiebcke, *Chem. Mater.* **2011**, *23*, 2130.
[22] Y.-D. Wang, C.-L. Ma, X.-D. Sun, H.-D. Li, *Nanotechnology* **2002**, *13*, 565.
[23] M. Zahmakiran, *Dalton Trans.* **2012**, *41*, 12690.
[24] X. Zhao, X. Bu, T. Wu, S.-T. Zheng, L. Wang, P. Feng, *Nat. Commun.* **2013**, *4*, 2344.
[25] A. Houas, H. Lachheb, M. Ksibi, E. Elalouui, C. Guillard, J.-M. Herrmann, *Appl. Catal. B* **2001**, *31*, 145.
[26] M. A. Nasalevich, M. van der Veen, F. Kapteijn, J. Gascon, *Cryst. Eng. Comm.* **2014**, *16*, 4919.
[27] H.-P. Jing, C.-C. Wang, Y.-W. Zhang, P. Wang, R. Li, *RSC Adv.* **2014**, *4*, 54454.
[28] L. H. Wee, N. Janssens, S. P. Sree, C. Wiktor, E. Gobechiya, R. A. Fischer, C. E. A. Kirschhock, J. A. Martens, *Nanoscale* **2014**, *6*, 2056.
[29] S. Wu, H. Cao, S. Yin, X. Liu, X. Zhang, *J. Phys. Chem. C* **2009**, *113*, 17893.
[30] C. Tian, Q. Zhang, A. Wu, M. Jiang, Z. Liang, B. Jiang, H. Fu, *Chem. Commun.* **2012**, *48*, 2858.
[31] T. Borjigin, F. Sun, J. Zhang, K. Cai, H. Ren, G. Zhu, *Chem. Commun.* **2012**, *48*, 7613.
[32] P. Horcajada, T. Chalati, C. Serre, B. Gillet, C. Sebrie, T. Baati, J. F. Eubank, D. Heurtaux, P. Clayette, C. Kreuz, J.-S. Chang, Y. K. Hwang, V. Marsaud, P.-N. Bories, L. Cynober, S. Gil, G. Ferey, P. Couvreur, R. Gref, *Nat. Mater.* **2010**, *9*, 172.
[33] J. Silvestre, N. Silvestre, J. De Brito, *J. Nanomater.* **2015**, *2015*, 106494.
[34] B. K. Kandola, D. Deli, in *Polymer Green Flame Retardants* (Eds.: C. D. Papaspyrides, P. Kiliaris), Elsevier, Oxford **2014**, pp. 503–549.
[35] J. Lim, S. Jun, E. Jang, H. Baik, H. Kim, J. Cho, *Adv. Mater.* **2007**, *19*, 1927.
[36] N. R. Jana, L. Gearheart, C. J. Murphy, *Langmuir* **2001**, *17*, 6782.
[37] M. Wu, G. Lin, D. Chen, G. Wang, D. He, S. Feng, R. Xu, *Chem. Mater.* **2002**, *14*, 1974.
[38] A. Kar, S. Kundu, A. Patra, *J. Phys. Chem. C* **2011**, *115*, 118.